

Sea and swell wave energy on the reef-fringed shoreline of Ipan, Guam

Anne-Christine Péquignet,

Department of Oceanography, University of Hawaii at Manoa,
1000 Pope Road, Honolulu, HI 96822, USA.
chrispeq@hawaii.edu

Janet M. Becker, Department of Geology and Geophysics, 1680 East West Rd, University of Hawaii at Manoa, Honolulu, HI 96822, USA.
jbecker@soest.hawaii.edu

Mark A. Merrifield,
Department of Oceanography, University of Hawaii at Manoa, 1000 Pope Road, Honolulu, HI 96822, USA.
(markm@soest.hawaii.edu)

Stanley J. Boc,
US Army Corps of Engineers,
4155 E. Clay Street,
Vicksburg, MS 39183, USA.
(Stanley.J.Boc@usace.army.mil)

Abstract Field observations of wave transformation during moderate and tropical storm conditions in Guam are used to parametrize wave breaking and bottom friction for Ipan reef. These parameterizations of dissipative processes are used in the integration of the sea and swell band energy flux equation across the reef for a range of incident wave conditions. The observed increase in wave setup and swell height on the reef flat with increasing incident wave energy is well reproduced by the dissipative energy flux model. The model is extended to assess the effects of larger tidal range and incident wave heights on swell band wave height at the shoreline at Ipan. It is shown that above a threshold of incident wave energy, the amount of wave energy that reaches the shore depends on the reef width and the reef top water depth, whether the submergence is due to tides, wave setup or general sea level variability.

Keywords: fringing reef, hydrodynamics, waves, wave setup, sea level, model, friction,

Introduction

Fringing reefs provide significant shoreline protection from incident wave energy. Incoming sea and swell energy dissipates strongly through the combined effects of wave breaking and friction, and wave driven inundation at the shore is significant only during large wave events.

Coastal inundation due to wave runup is composed of the increased mean water level at the shoreline caused by wave setup (Bowen et al 1968; Tait 1972), and oscillations about this setup (swash) associated with wave energy that reaches the shore (Guza et al 1984). The present study is aimed at determining the amount of sea and swell energy available for runup at the shoreline of a reef fringed beach for various wave and tidal conditions and compare it to results for sandy shores beaches (e.g., Raubenheimer et al 1995a; Raubenheimer and Guza 1996; Holman and Guza 1984; Ruggiero et al 2004; Stockdon et al (2006)).

Wave runup may be seen as the result of a series of transformation processes as waves propagate towards shore. These transformation processes on various reef geometries have been the focus of many studies (e.g., Tait 1972; Gerritsen 1981; Young 1989; Gourlay 1996a; Hardy and Young 1996; Kench 1998; Lowe et al 2005; Kench and Brander 2006) and Monismith (2007) provides an excellent overview of reefs hydrodynamics. Studies of reef scale motions typically involve the depth-integrated momentum flux associated with propagating waves, or radiation stress (Longuet-Higgins and Stewart 1962). As incident waves break at the reef face, gradients of radiation stress force pressure gradients resulting in the setup of the sea surface (Gourlay 1996a; Gourlay 1996b; Vetter et al 2010), and mean currents across the reef (Symonds et al 1995; Gourlay and Colleter 2005). As the incident waves propagate into shallow water on the reef flat, they also are increasingly affected by frictional effects. On some barrier reefs, friction has been shown to be the dominant dissipative process (Lowe et al 2005).

On many reefs, however, wave transformation observations show that breaking often accounts for the majority of the dissipation of waves in the sea and swell (SS) frequency band (0.04 to 0.3 Hz) (Young 1989; Hardy and Young 1996). Time varying wave breaking has been suggested as a generation mechanism for low frequency oscillations at infragravity (IG) frequencies (0.005 to 0.04 Hz) and possibly far infragravity (fIG) frequencies (0.0001 to 0.005 Hz) and provides an explanation for the broadening of the energy spectrum observed across reefs (Young 1989). Observations show that, the inshore region of shallow reef flats, similar to the swash zone of dissipative sandy beaches, tends to be dominated by long waves at IG frequencies (e.g., Young 1989; Lugo-Fernandez et al 1998b).

The transmission of sea and swell energy toward shore is affected by the tide, with increasing wave energy on reef flats observed for increasing tidal level (Young 1989; Hardy and Young 1996; Lugo-Fernandez et al 1998a; Brander et al 2004). During large wave events, wave setup contributes to the water level increase on the reef with level changes that may exceed the highest tidal range (Péquignet et al 2009). As most observational studies to date have captured only moderate wave events, open questions remain regarding reef flat energy levels during large wave events that generate significant setup.

The goal of this paper is to analyze field observations of waves across a fringing reef, in an effort to predict the amount of sea and swell energy that reaches the shore as a function of incident wave conditions and water level over the reef. We first detail the field experiments at Ipan and then present a spectral description of wave energy across the reef, which highlights the relative importance of the two distinct frequency bands, sea and swell (SS) and infragravity (IG). The transformation of sea and swell energy is then detailed and leads to the development of an observationally-based model study that assesses how a range of incident conditions affects the amount of SS wave energy that reaches the shore.

Field experiment and analysis

Data used in this study were collected as part of the Pacific Island Land-Ocean Typhoon (PILOT) project which is aimed at assessing coastal inundation at reef-fringed islands during large wave events. The study site at Ipan (Fig. 1), on the south shore of Guam ($13^{\circ} 22'20''\text{N}$, $144^{\circ} 46'30''\text{E}$), is composed of a narrow sandy beach connected to a shallow 450 meter wide reef platform composed of carbonate pavement covered by macro algae (Fig. 2). The porous reef crest is composed of aggregate reef covered by macro algae and coralline algae, and is extended by a 100 meter wide spur-and-groove coral structure down to a depth of approximately 15 meters (Burbick 2005). The tides in Guam are mixed semi-diurnal with a mean range of 0.5 m and spring tide range of 0.7 m. The reef flat is mostly exposed at low tide. The eastern side of Guam is exposed to trade winds and subjected to occasional tropical storms and typhoons (Lobban and Schefter 1997) which have been responsible for large and variable wave overwash along the south shore of Guam (Jaffe and Richmond 1993). Typical trade wind waves have periods ranging between 7 and 12 seconds, but occasional storm events result in swell of periods greater than 14 seconds. Typical offshore significant wave heights are between 1 and 2 meters, with wave heights reaching 4 meters during winter storms.

A cross-shore array of Seabird SBE 26Plus wave and water level recorders and Nortek Aquadopp Acoustic Doppler Velocimeters (ADV) was deployed across the reef, with two instruments offshore of the reef crest and the remainder on the reef flat (Fig. 1). Deployments of 3 to 6 months of varying number of instruments and sampling schemes were carried out from August 2005 and April 2010. The 2 subsets of data used in this study were collected between September 2009 and November 2009 (deployment N) and between June and July 2007 (deployment G). During deployment N, the ADVs sampled at 1 Hz in bursts of 2 hours every 3 hours. During deployment G, the ADVs sampled at 1 Hz in bursts of 2 hours every 4 hours. During both deployments, the SBE 26Plus sampled at 1 Hz in bursts of 43,180 seconds every 12 hours.

Pressure measurements are corrected for atmospheric pressure variations using a SBE 26Plus deployed on land (sensor atm P on Fig. 1). Using linear wave theory, sea surface elevations are estimated from bottom pressure and surface velocities are calculated from mid-column velocity. Changes in water temperature on the reef account for uncertainties of less than 0.2% in the estimation of sea surface elevation from the pressure sensors. Using pressure data, the times when the reef flat instruments were not submerged were flagged and are not considered in the present analysis. Offshore conditions are given by a CDIP operated Datawell directional wave buoy located 2.4 km southeast of the reef array ($13^{\circ} 21'15''\text{N}$, $144^{\circ} 47'18''\text{E}$) in 200 meters of water.

The conditions during the two deployments are characterized by sea level, significant wave height, peak period and wave direction (Fig. 3). During deployment N, typical trade wind conditions generated incident wave heights up to 4m at our most offshore sensor. Typical wave peak periods range from 5 to 15 seconds with a few events reaching 20 seconds. The wave direction of typical trade wind waves is ENE but occasional events bring waves with a E or ESE direction. Deployment G was during calm summer conditions and an energetic storm event with offshore wave heights of approximately 8 m (9 July 2007), peak period of 11 seconds arriving from the SE, when tropical storm (later upgraded to typhoon) Man-Yi passed 200 nm south of Guam. The large waves observed during this event were responsible for high setup on the reef (Péquignet et al 2009; Vetter et al 2010), and inundation along some parts of the south shore of Guam.

For both deployments the incident significant wave height and peak period (Fig. 3) are specified using the most offshore instrument location (sensor new8, ~ 8 m depth). Wave heights experience approximately a 30% decrease in wave height between the offshore buoy and sensor new8 for waves incident from the South, presumably due to refraction effects. For long period swell (>12 seconds) and for waves incident from the north, however, some shoaling is observed between the buoy and the 8m

depth sensor.

Across the reef, 15-minute average significant wave heights are estimated from the variance of sea surface elevation in the SS band ($f_1=0.04$ Hz $< f < f_2=0.3$ Hz), in the IG band ($f_1=0.005$ Hz $< f < f_2=0.04$ Hz) and in the fIG band ($f_1=0.0001$ Hz $< f < f_2=0.005$ Hz) by

$$H_s = 4 \left(\int_{f_1}^{f_2} S_{\eta\eta}(f) df \right)^{0.5} \quad (1)$$

where $S_{\eta\eta}(f)$ is the autospectra of the sea surface elevation η .

Following Vetter et al (2010), setup on the reef flat is estimated at reef flat sensors by taking the difference of the 15-minute mean water level between the given sensor and sensor new8 and regressing this difference against the wave height at sensor new8, time (to account for any instrumental drift) and a constant. Setup is estimated by subtracting the time drift and the offset of the regression from the difference in water level. (see Vetter et al (2010) section 3.1)

Waves and water level

Representative time series of sea surface elevation at four cross-shore locations illustrate the change in wave form across the reef during small (Fig. 4 left: 22 July 2007 13:11:00) and large (Fig. 4 right: 9 July 2006 04:23:00) incident wave conditions (Fig. 4). A sharp shoreward decay in wave amplitude is observed near the reef crest (Fig. 4) with additional but more moderate attenuation on the reef flat. At sensors new8 to new6, the sea surface elevation is dominated by sea and swell oscillations at 5 to 10 seconds periods. Inshore of sensor new5, and in particular near the shoreline (sensor 1), the sea surface elevation is dominated by oscillations at periods of minutes (Fig. 4 c, d, g and h). This shoreward shift to longer period on the reef has been reported previously (Hardy and Young 1996; Lugo-Fernandez et al 1998a).

The cross-reef change in the power spectral density of sea surface elevation is illustrated for the small (Fig. 5 left: 22 July 2007 13:11:00) and large (Fig. 5 right: 9 July 2006 04:23:00) wave events. The shoreward decay of SS energy and increase in IG energy clearly are observed during both events. In particular, on the reef flat (from sensor new5 to 1), IG oscillations are more energetic than SS oscillations. Time series of mean water depth and significant wave height in the SS, and low frequency (IG+fIG) band presented for sensor 1 (Fig. 6). The water level on the reef at sensor 1 includes both tidal and wave setup components (Fig. 6 a and d). During large wave events, the setup on the reef exceeds the tidal range. The modulation of wave height with water depth on the reef is clearly observed for both the SS and low frequency significant wave heights with up to 10% of SS wave height from sensor new8 reaching sensor 1 at high tide and as low as 1% reaching sensor 1 at low tide (with an average of 3% for all water depths).

Analysis of sea and swell energy band

Energy flux and reflection

We next analyze the strong dissipation of SS waves during moderate and large wave events and quantify the processes involved. Incoming and outgoing energy fluxes may be estimated from the pressure and collocated cross-shore velocity assuming normal incidence following Shereme (2002). The normal incidence assumption is justified as the angle of incidence at the most offshore current-

meter location (Fig. 3 **d** and **h**), is always within 15° of shore normal due to wave refraction. The onshore (F_x^+) and offshore (F_x^-) energy flux densities at frequency f are estimated from the sea surface elevation η and cross-shore velocity u according to (Sheremet [2012](#)),

$$F_x^\pm(f) = \frac{1}{4} c_g(f) \rho g \left[S_{\eta\eta}(f) + (2\pi f / gk)^2 S_{uu}(f) \pm 2(2\pi f / gk) S_{\eta u} \right] \quad (2)$$

where ρ is the water density, g is the acceleration due to gravity, $c_g(f)$ is the group velocity, $S_{\eta\eta}(f)$ is the co-spectrum of η and u , and $S_{\eta\eta}(f)$ and $S_{uu}(f)$ are the auto-spectra of η and u , respectively.

We compute the ratio of offshore to onshore energy flux $R^2 (= F_x^- / F_x^+)$ at each collocated pressure and current-meter sensor location when all parts of the reef are submerged. [Not](#) estimated on the reef flat when any part of the reef is exposed. Errors resulting from the assumption of normal incidence lead to the overestimation. In addition, as shown by Huntley et al (1999), the possible error introduced by noise in the data and the subsequent decrease of coherence between sea surface elevation and velocity also will introduce a positive bias. R^2 at both sensor locations exhibits the strong dependence on frequency observed on sloping beaches (Elgar et al 1994) (Fig. 7). For low frequency band waves, R^2 varies between 1.1 and 0.2 with an average value of 0.5 at the reef face and ranges between 0.1 and 0.5 on the reef flat.

In the SS band, reflection is much weaker and varies between 0.05 and 0.1 (Fig. 7) with an average value approximating 0.06. The low value is largely due to SS wave dissipation from breaking and friction. On the reef flat and at the reef face, reflection in the SS band presents small variations associated with changes in water depth. On sandy beaches, the dependence of SS reflection with tidal elevation has been attributed to changes in beach slope as a function of tidal height (Elgar et al 1994; Okihiro and Guza 1995). In contrast, for fringing reef topography, the dependence of reflection at the reef face on tidal elevation appears to be related to the submergence of the reef following formulations of reflection and transmission of wave energy at a topographic step (Bartholomeusz 1958; Kajiura 1961; Newman 1965; Mei 1989). Reflection at a discontinuous [inviscid](#) step, however, only depends on the water depth on both sides of the step. The frequency dependence of R^2 (Fig. 7) suggests that Ipan reef behave like a step with smooth continuous transition. This is confirmed by the good agreement (Fig. 7) between observed reflection coefficient at the reef face and the theoretical reflection of Kajiura (1961) at a smooth step modeled by

$$h(x) = \left(\frac{1}{2} \left(\frac{1}{h_1} + \frac{1}{h_2} \right) - \frac{1}{2} \left(\frac{1}{h_1} + \frac{1}{h_2} \right) \tanh\left(\frac{nx}{2}\right) \right)^{-1} \quad (3)$$

where h_1 and h_2 are the depth on and off the step, and nx represents the width of the transition (equations 76 of Kajiura (1961)). [The](#) departure from Kajiura's solution and large values of reflection coefficient at low frequencies and values above 1, suggest that outgoing low frequency waves may have been generated through non-linear processes at the reef edge.

Given the small amount of reflection in the SS band, we assume that SS oscillations are predominantly in the form of onshore propagating waves and estimate the cross-shore energy flux at locations where cross-shore velocity is not available according to

$$F_x(f) = \frac{1}{2} c_g(f) \rho g S_{\eta\eta}(f) \quad (4)$$

Equation (4) follows from (2) for normally incident incoming progressive linear waves. This assumption makes possible the computation of energy flux at locations where velocity data are not available. The error associated with this assumption was estimated by comparing the onshore energy flux estimated with equation (2) and the net flux estimated with equation (4). The error increases with increasing wave energy and was observed to be at most 29%.

We next present an overview of the energy flux for three distinct regions of the reef: the reef face (sensors new8 and new7), the reef edge and crest (sensors new7 to new5), the reef flat (sensors new5 to 1).

For the sea and swell frequency band, the energy flux between sensor new8 and new7 is conserved except during large events where a small decrease in energy flux is observed at sensor new7 (Fig. 8). Based on shallow water breaking criteria (Mei 1989), the decrease in energy flux for the largest waves may be due in part from wave breaking. Reported breaker height to depth ratios vary from 0.4 to 1.8 for sandy beaches and reef slope ranging from 0.02 to 0.12 (Bowen et al 1968; Tait 1972). For depth-limited breaking to occur on the reef face at Ipan, we estimate that significant wave heights at sensor new7 must exceed 3.2 m, which only was observed during the peak of tropical storm Man-Yi. At the reef edge (between sensors new7 and new6), the pronounced decrease in energy flux is due to wave breaking. Visual observations confirm that the surf zone is confined to a narrow zone around the reef edge. A slight increase in energy flux is observed occasionally between sensor new6 and new5 (Fig. 8) but may not conclusively be attributed to a dynamical process as the difference in energy flux lies within the error bars. On the reef flat (between sensors new4 and 1), the small decrease in the remaining energy flux shoreward of the surfzone appears to result from bottom friction (Lowe et al 2005). This energy flux reduction is greater at low tide. Sea and swell wave attenuation for incident wave heights >1m is very strong on the reef with less than 3% of the incident energy flux reaching sensor new4, and less than 0.3% reaching sensor 1, even at high tide. These reductions in SS energy flux are consistent with previous studies (e.g. Young 1989; Kench 1998; Lugo-Fernandez et al 1998a; Brander et al 2004).

Energy flux divergence

Neglecting longshore components of energy flux, the energy flux divergence in the sea and swell band may be written as

$$\frac{dF_{SS}}{dx} = -\langle \varepsilon_b \rangle + \langle \varepsilon_f \rangle + \langle N \rangle \quad (5)$$

where the SS energy flux F_{SS} is estimated by integrating the energy flux density over the SS frequency band, and $\langle \varepsilon_b \rangle$ and $\langle \varepsilon_f \rangle$ are the average rate of dissipation per unit area due to wave breaking and bottom friction respectively, and $\langle N \rangle$ is the non-linear transfer of SS energy to other frequency bands. Non-linear transfer of SS energy to higher frequencies has been observed on a reef during small wave conditions (Hardy and Young 1996). At Ipan, the generation of small wavelets after breaking (of period non-resolvable by our sampling scheme) have been visually observed near the reef crest but only during small incident waves. In addition, no significant high frequency peak of energy is observed in the spectrum of sea surface elevation on the reef flat.

The increase in IG energy from the reef face to the reef flat and the occasional observation $R^2 > 1$ at the reef face suggests that low frequency oscillations are generated locally. Two important mechanisms for the generation of IG waves are quadratic difference interaction among pairs of incident waves producing a forced or bound wave that is released at the break point, and the generation of IG waves by time variable gradients of radiation stress (Schaffer 1993). As a result, we expect that the majority of

the low frequency wave generation will occur on the steep reef face where breaking occurs, and we may neglect $\langle N \rangle$ in the SS balance (5) on the reef face before breaking occurs (offshore of sensor new7) and on the reef flat after breaking (inshore of sensor new4).

From our observations, the contribution of SS energy toward the generation of IG energy is estimated by comparing the energy flux divergence in the sea and swell band (dF_{SS}/dx) to the energy flux divergence in the IG band (dF_{IG}/dx) in each of the three regions. Because reflection in the IG band is not negligible (Fig. 7), we estimate both onshore and offshore IG energy flux divergences at sensor locations where velocity data are available (sensors new8, new7, new5, new3 and 1 for N deployment, sensors new7 and new5 for G deployment, see Fig. 1).

On the reef face, between sensors new8 and new7, and at the reef crest, between sensors new7 and new5, the decrease of SS energy flux is much larger than the rate of increase in IG energy flux, and although $\langle N \rangle$ is important in the IG energy balance, it may be neglected in the SS energy balance (5). Inshore of the break point, (from sensor new5 to sensor new3 for N), the rate of change of energy flux in the SS band is comparable to the rate of change of energy flux in the IG band. This suggests that dissipation may not only be due to breaking and friction and that some energy may be transferred between the SS and IG band, therefore $\langle N \rangle$ may not be negligible in the SS energy balance between sensors new5 and new3. On the reef flat (between sensor new3 to new1) energy in both SS and IG bands is dissipated.

For regions of the reef where $\langle N \rangle$ may be neglected (offshore of sensor new5 and inshore of sensor new3), we compare the cross-shore energy flux divergence in the sea and swell band with existing parametrizations of dissipation based on significant wave height. Offshore of the reef crest and on the reef flat (Fig. 9 a and c) the dependence of the SS energy flux divergence dF_{SS}/dx with significant wave height is approximately cubic, while near the reef crest (Fig. 9 b) the dependence is quadratic. For deployment G, when no sensors were deployed at location new3, we use sensor new4 and the dependence of energy flux divergence on H_{rms}^3 from sensor new3 to 1 for N and from new4 to 1 for G are the same (Fig. 9 c).

We next compare the flux divergences and the implied dissipation rates in three regions (reef face from sensor new8 to new7, reef crest from sensor new7 to new5, the reef flat from sensor new4 to 1) to existing models of wave breaking and bottom friction developed for sandy beaches.

Wave breaking

While parametrizations of the energy lost to turbulence due to wave breaking have not been developed specifically for fringing reefs such as Ipan, sloping beach parametrizations have been successfully applied to reefs (Young 1989; Massel and Gourlay 2000). Wave breaking parameterizations have been developed based on laboratory (eg. Battjes and Janssen 1978) and field observations (eg. Thornton and Guza 1983). The approximation of a breaking wave as a propagating bore (LeMéhauté 1962) has been widely used with satisfactory results. The rate of dissipation due to wave breaking, ϵ_b modelled as a bore connecting two region of uniform flow (Stoker 1957; LeMéhauté 1962; Battjes and Janssen 1978; Thornton and Guza 1983), is derived by applying conservation of mass and momentum upstream and downstream of the bore and may be written as

$$\epsilon_b = B/4 \rho g f H^3 / h \quad (6)$$

where f is the wave frequency, H is the wave height, and B is an empirical coefficient of $O(1)$ representing the fraction of foam on the wave face.

For a random wave field, the average rate of dissipation $\langle \epsilon_b \rangle$ is obtained by assuming a probability

distribution for the wave field and applying (6) to the broken waves only. The distribution of breaking wave height typically is taken as a truncated Raleigh distribution (Thornton and Guza 1983). Following Thornton and Guza (1983) (their equation 25) and with the saturated wave field assumption that $H_b/h=O(1)$ near breaking (Baldock et al 1998), the average rate of dissipation reduces to a quadratic function of $H=H_b$

$$\langle \varepsilon_b \rangle \approx B_r \rho g \bar{f} H_b^2 \quad (7)$$

where \bar{f} is the representative frequency of the random wave field and B_r is a constant factor.

On the reef crest, between sensors new7 and new5, the observed quadratic dependence of the energy flux divergence with incident wave height (Fig. 9 b) suggests dissipation due to breaking following the model of a saturated surfzone (7). We estimate the breaking parameter B_r by assuming that frictional dissipation between sensors new7 and new5 is negligible compared to the breaking dissipation. We show that this assumption is valid in the following section. A least squares fit to the data in Fig. 9 b suggests that $B_r = 0.075$ which is equivalent to the value used by Young (1989) with a similar parametrization of breaking. This parametrization of breaking as a propagating bore does not account for the very porous nature of the bottom but the value of B_r may implicitly incorporate this effect.

Friction

The rate of energy dissipation of monochromatic waves due to friction, ε_f may be defined as the work done by the wave orbital velocity against the shear stress at the seabed. In the drag law model, the maximum bed shear stress τ is expressed as $\tau = \rho C_f | \mathbf{u}_b | \mathbf{u}_b$ (Jonsson 1966), resulting in

$$\varepsilon_f = \tau \mathbf{u}_b = \rho C_f | \mathbf{u}_b | \mathbf{u}_b^2 \quad (8)$$

where u_b is the instantaneous near bed velocity, and C_f is the bed friction coefficient. For a monochromatic or narrow band wave field, the orbital velocity may be expressed as a function of wave height and frequency assuming linear wave theory. Thornton and Guza (1983) derived the following expression for the average rate of frictional dissipation $\langle \varepsilon_f \rangle$ for a field of random waves using a Rayleigh probability distribution for the waves

$$\langle \varepsilon_f \rangle = \rho C_f \frac{1}{16\sqrt{\pi}} \left(\frac{2\pi \bar{f}}{\sinh kh} \right)^3 H_{rms}^3 \quad (9)$$

where h is the water depth, \bar{f} is the representative frequency of the random wave field, k is the wave number associated with \bar{f} given the water depth, and $H_{rms} = \frac{1}{\sqrt{2}} H_s$ is the root mean square wave height.

The energy flux divergence on the reef face (between sensors new8 and new7) is best fit with cubic wave height dependence, consistent with equation (9). On the reef flat, the energy flux divergence is estimated between sensor new4 and 1 for deployment G and sensor new3 and 1 for deployment N

where a pressure sensor was deployed at the location 4. Nevertheless, both divergences are best fit with cubic wave height dependence and with a similar slope (Fig. 9 c). A least squares fit of the data (Fig. 9) yields a friction coefficient of $C_f = 0.06 (\pm 0.02)$ on the reef flat. On the reef face, the friction coefficient is estimated to be $C_f = 0.2 (\pm 0.05)$. The uncertainties associated with the C_f values are 95% confidence intervals of the regression from Fig. 9. Young and Gorman (1995) note that, an equivalent expression for the maximum bed shear stress $\tau = 1/2 f_w \rho |u_b| u_b$ often is used, where f_w is the wave friction factor, and $C_f = 1/2 f_w$. The present estimates of friction coefficients show good agreement with values of f_w on other reefs (eg. $f_w = 0.1$ to 0.7 , Ala Moana (Gerritsen 1981); $f_w = 0.1$ - 0.7 , Ala Moana, Ningaloo (Hearn 1999); $f_w = 0.07$ to 0.22 , John Brewer reef (Nelson 1996); $C_f = 0.03$ to 0.1 , Kaneohe (Hearn 1999))

Additionally, the friction factor $f_w = 2 C_f$ has been related to bed hydraulic roughness or equivalent Nikuradse roughness height, r , (Swart 1974; Mirfenderesk and Young 2003). For a fully rough turbulent flow, Swart (1974) provides the following explicit formulation for f_w ,

$$f_w = \exp(5.213 \left(\frac{r}{a}\right)^{0.194} - 5.977) \quad (10)$$

where a is the wave orbital diameter at the bed. Assuming linear waves in the shallow water limit yields $a = H_{rms}/(2kh)$, with k the local wave number.

During the peak of Man-Yi, using the average value of $C_f = 0.2/0.06$ and equation (10) yields a roughness $r \approx 1$ m/17 cm on the reef face/reef flat. Based on visual observations of the spur and groove structure on the reef face (Fig. 2), the roughness scale of 1 m is reasonable. On the reef flat, a representative value of 17 cm is reasonable for Ipan and comparable to roughness estimates on other similar reefs (Nelson 1996, Nunes and Pawlak 2008).

The relationship between friction factor and wave orbital diameter of (10) suggests that for a given roughness and wave period, the friction factor increases for increasing wave height and decreasing depth on the reef. This increase is particularly pronounced for small waves with small orbital amplitude. As a consequence, the friction factor is likely to be larger for small waves. At the reef crest, the roughness scale appears to be between the roughness scale of the reef face and that of the reef flat (Fig. 2) and using equation (10), for an intermediary value of roughness of 60cm, we estimate the friction factor of the reef crest as 0.13. For this estimate of C_f , the frictional dissipation estimated between sensors new7 and new5, is small compared to the total dissipation (less than 2% for small wave conditions and at a maximum of 7% at the peak of Man-Yi), confirming that friction may be neglected with respect to breaking between sensors new7 and new5.

Model of energy flux transformation

Model description

The frictional and breaking parameterizations discussed above now are used to a numerical integration of the momentum and the sea and swell energy flux equation across the reef (from sensor new8 to sensor 1) using an explicit forward scheme. Inputs for the calculation are the reef bottom topography (Fig. 1), the 15-minute mean tidal level d , incident significant wave height, H_s , and peak period, T_p , at sensor new8. A summary of parameters and input variables used for each model run are summarized in Table 1. The energy flux equation (5) is integrated with the bottom friction term ϵ_f estimated from equation (9) specified at every cross-shore point, the breaking term ϵ_b (estimated from equation (7))

included in regions where the breaking criterion is met ($H_s \geq \gamma_b h$, $\gamma_b=1.15$), and the non linear term is neglected everywhere yielding,

$$\frac{dF_{SS}}{dx} = \rho C_f \frac{1}{16\sqrt{\pi}} \left(\frac{2\pi \bar{f}}{\sinh kh} \right)^3 H_{rms}^3 + H(H_s - \gamma_b h) B_r \rho g \bar{f} H_b^2 \quad (11)$$

where H is the Heaviside step function.

The validity of neglecting the non linear term inshore of the breakpoint will be discussed in the next section. At each spatial increment ($dx=1$ m), the total depth is given by $h = d + \bar{\eta}$, where d is the tidally varying water level, assumed spatially constant across the reef, and $\bar{\eta}$ is the wave setup which varies across the reef. Setup is computed using a 4th-order Runge-Kutta scheme to solve the mean momentum equation

$$\frac{\partial \bar{\eta}}{\partial x} = - \frac{1}{\rho g (\bar{\eta} + d)} \frac{\partial S_{xx}}{\partial x} \quad (12)$$

where S_{xx} is the cross-shore radiation stress (Longuet-Higgins and Stewart 1964). At each time and space iteration, the cross-shore SS energy flux F_{SS} is used to compute the total SS energy E_{SS} , the significant wave height H_s and the cross-shore radiation stress S_{xx} following

$$F_{SS} = c_g E_{SS} = \frac{1}{16} c_g \rho g H_s^2 \quad (13)$$

$$S_{xx} = E_{SS} \left(2 \frac{c_g}{c} - \frac{1}{2} \right) \quad (14)$$

c_g and c are the local group velocity and phase speed, at the peak SS frequency.

The choice of breaking criteria with respect to significant wave height $\gamma_b = 1.15$ is taken from the reported range of 0.4 to 1.8 (for a range of slope of 0.02 to 0.12) (Bowen et al 1968; Tait 1972; Raubenheimer et al 1996, Vetter et al 2010), given the average reef face slope at Ipan of 0.07. We use $C_f = 0.2$ on the reef face and crest, and 0.06 on the reef flat.

Performance of the model

The modeled and observed H_s and $\bar{\eta}$ closest to shore (sensor 1) compare well for deployments N and G (Fig. 10). The correlation of observed and modeled H_{s1} ($\bar{\eta}_1$) is 0.89 (0.98) for deployment N and 0.97 (0.98) for deployment G.

During large incident wave conditions, the model underestimates the observed setup by about 30% (Fig. 10). The underestimate of setup during large wave conditions may result in part from errors in computing S_{xx} over the steep reef face and in part from neglecting the friction term in the momentum

equation. The model predicts wave heights very well for large wave conditions but for small incident wave conditions, for which data were not used in the estimation of the dissipation parameters, the model overestimates the wave height H_{sl} by up to a factor 2. This overestimation during small wave conditions, is in part due to the assumption of a constant friction coefficient and in part due to the overestimation of setup by the model which increases the total depth. Additionally, the depth-limited breaking criteria may underestimate breaking on the steep face for small waves and high tide conditions, leading to an overestimation of wave height on the reef flat for these conditions.

Sensitivity to parameters

The roughness of the reef decreases shoreward (from meter scale on the reef face to tens of centimeters scale on the reef flat, Fig. 2) and the friction coefficient is likely to also increase gradually from the reef face to the shore. However, the friction coefficient is only estimated for two distinct regions of the reef and the reef face value is used at the reef edge. This may be responsible for the difference between the observed and the modeled significant wave height at sensor new6 (Fig. 11) where the estimated friction value of the reef face likely overestimates the real value.

The similarity parameter (or ratio of H_{rms} to depth) at sensor new6 is estimated to be 1.4 (Vetter et al 2010). This corresponds to a ratio of significant wave height H_s to depth of 1.4 assuming that most of the breaking dissipation occurs at one cross-shore location Vetter et al (2010) successfully modeled wave setup with this value as breaking criteria. The present model assumes a finite surfzone width.

Breaking is likely to also occur offshore of sensor new6. For this to happen the breaking criteria γ_b has to be smaller than 1.4 to initiate breaking in deeper water. We choose a value of γ_b of 1.15 (or $0.8 \gamma_b$ to H_{rms}), which corresponds to values previously used on reefs (Young 1989). Integrated over the cross-shore width of the reef face, this value of breaking criteria over a finite surfzone or the single breakpoint of Vetter et al (2010) with larger γ_b gives similar setup estimation.

This value γ_b corresponds to the value that gives best fit with observations with the value of B_r estimated from the observations (Fig. 10 and Fig. 11 a). The value B_r and γ_b are related and to achieve the same amount of breaking dissipation with a larger B_r , γ_b would have to be larger to dissipate wave energy over a smaller distance.

Despite the discrepancy between model observed wave height on the reef face, the depth-limited breaking criteria accounts for all the dissipation over the entire length of the reef (Fig. 11 b). This sharp dissipation around the reef edge may result from the choice of a constant value of γ_b . Following Raubenheimer et al (1996) the value of γ_b should be larger on steeper slope. This means that γ_b should be larger on the reef face than on the reef flat. For larger waves breaking further on the slope, γ_b should also be larger than for smaller wave breaking closer to the reef crest. Neglecting the non linear term inshore of sensor new7 in the energy flux balance (11) may also explain some of the difference between the observed gradual cross-shore decay and the less gradual modeled decay of wave height at the reef face for large waves (Fig. 11 b).

Wave setup is related to γ_b (Tait 1972; Vetter et al. 2010), and an error in γ_b may explain why setup is slightly overestimated for small waves while being underestimated at the peak of Man-Yi (Fig. 10).

Model simulations for ranges of wave and topographic conditions

Effect of changing water level, incident wave height and wave period

We next use (11)-(14) with fixed parameters (see Table 1-indep. increase), to investigate the effect

of independently changing incident wave height (H_{s8}), incident wave period (T_8) and tidal level (d) on the shoreline significant wave height H_{s1} and setup $\bar{\eta}_1$ (Fig. 12).

For a given incident wave height and period, raising the tidal level increases the wave height on the reef (Fig. 12, left panel). This strong increase in H_{s1} occurs with a moderate decrease in setup associated with a reduction of wave breaking.

The wave height on the reef flat also increases with increasing incident wave height (Fig. 12, middle panel). This near linear increase of reef flat wave height is in part due to the increase of water depth on the reef from a nearly linear increase in wave setup (Fig. 12e). The increase of wave height on the reef with incident wave height and water depth has been previously reported (Young 1989; Hardy and Young 1996; Lugo-Fernandez et al 1998c) for barrier reefs under moderate conditions.

We find a moderate increase of both setup and wave height near the shore for a linear increase in incident wave period from 5 to 20 seconds (Fig. 12, right panel). Long waves experience less dissipation (both breaking, (7) and friction, (9)) than short waves; hence, reef flat wave heights increase with wave period. The dependence of setup on wave period previously reported for reef lagoon system (Hench et al 2008) is observed at Ipan, where setup scales as $T^{0.25}$.

Importance of water depth on the reef

We next focus on model estimates of nearshore wave height for a tidal range larger than that observed at Ipan. Input of a simulation with co-varying tidal level and incident wave height are summarized in Table 1 (co-varying) and shown in Fig. 13.

The wave height near the shore is nearly constant for a given water depth on the reef regardless of whether the water depth is determined by wave setup or tides (Fig. 13 a). Over a minimum incident wave height threshold for a given depth on the reef, the wave height at the shore is nearly independent of the incident wave height (Fig. 13 b). The threshold value is related to the shallowest depth observed at the reef crest; for waves smaller than γ_b times this depth no breaking will occur and the wave height on the reef flat does not differ from the incident value. This suggests that water depth on the reef strongly controls the amount of SS energy that reaches the shore in agreement with wave dissipation being dominated by a depth limited breaking process. Increasing the water level allows larger incident waves to penetrate the reef flat.

Setup is predominantly controlled by incident wave height and is only weakly affected by water level changes. Wave height at the shoreline increases with water depth on the reef with an exponent of 1.42. The only dependence of wave height at the shore with incident wave height comes from the linear dependence of setup on incident wave height. Details on the dependence of setup and reef flat wave height with incident wave heights, water levels and wave periods are summarized in the appendix.

Effect of reef topography

To test how the roughness of a given reef influences the wave height on the reef, we increase and decrease the friction coefficient from 0 to 4 times the estimated values (Table 1-var. Cf).

Reef flat wave height increases more rapidly with water depth as friction is increased (see Appendix). The amplitude of the reef flat setup is not affected significantly as friction is not included in the setup momentum balance.

The model of energy flux transformation defined in model description section is applied to a reef with similar topography on the neighboring island of Saipan. Saipan reef in Laulau Bay (15° 09'38"N, 145° 45'11"E) has a slightly steeper slope than Ipan and a similar but narrower flat reef top of width ~135 m (Fig. 14). Pressure data across the reef were collected during the same Man-Yi deployment

(June-July 2007) at a depth of 11 m on the reef face and in the middle of the reef flat in a mean depth of 40 cm (Vetter et al 2010). The tides in Saipan are similar to the tides at Ipan and the reef also is exposed at low tide.

As SHOALS bathymetry data are not available for Saipan, the reef topography at Laulau Bay is approximated from the Guam topography by adjusting the Ipan bathymetry with the four known locations on Saipan: the two sensor locations at a depth of 11m and at the 40 cm deep mid reef location, and at the two visually distinct topographic features: the reef edge and the shoreline. The incident conditions observed at a depth of 11m are used as input in the transformation model (11)-(14). From visual observations, the roughness of the reef appears similar to Ipan and the Ipan friction coefficients are used on the scaled cross-shore profile. Breaking parameters are taken from the Ipan data but because the reef face is steeper, the breaking criteria which is strongly dependent on the slope (Tait 1972) is increased to $\gamma_b = 1.2$. Fig. 14 shows the estimated reef bathymetry, and the comparison between data observed at the mid-reef location and estimates from the model (Table 1-Saipan). Correlation between observed and modeled wave height (water depth) is 0.92(0.95) respectively. The model provides a reasonable estimate of the observed setup but like Ipan, underestimates the setup at the peak of the storm (Fig. 14). The mid reef wave height is well reproduced when the incident wave heights are larger than 1 m, but the model underestimates wave height for small incident wave conditions. This is consistent with the estimate for Ipan, where the model underestimates wave height closer to the reef edge (Fig. 11). We evaluate the model at a cross-shore location equivalent to that of sensor 1 for Ipan to estimate the shoreline wave height and setup at Saipan. During the Man-Yi deployment, an average of 8% (and a maximum of 25%) of the SS wave height reaches the location near the shore at Saipan. This is in comparison to an average of 3.5% (and a maximum of 10%) at Ipan. Next, the model response to variations in reef flat width for a fixed friction factor is examined by increasing the reef flat width of Ipan to 1200 m (see Table 1-var. L). For the given reef face topography, a wider reef allows for more wave attenuation and the mean and maximum ratio of wave height that reaches the shore to incident wave height decreases nearly inversely with increasing reef flat width as expected (Jaffe and Richmond 1993) (See Appendix). This is consistent with the larger ratio of shoreline to incident wave height at Saipan compared to Ipan. We find that reef width does not affect setup significantly and speculate that, as suggested by Thompson and Hamon (1980), the width of the reef may instead influence the amount of time needed for the setup balance to be established.

Conclusions

The dissipation of SS waves on the fringing reef of Ipan is analyzed in terms of the cross-shore transformation of energy flux. This strong dissipation, resulting in a 90% reduction of the incident wave height over ~500 m, from the most offshore to the most inshore sensor, is dominated by wave breaking (>80% of the dissipation). The remaining dissipation is provided by bottom friction on the rough substrate.

Previous wave breaking and frictional parameterizations developed on sandy beaches prove useful to represent the dissipation on the reef. Wave data collected for a range of incident conditions are used to estimate friction and breaking parameters for this reef.

Estimates of the friction factor on the reef vary across the reef (C_f from 0.06 to 0.2) and also with incident wave conditions. It appears that a roughness parametrization, such as Swart (1974), may be more appropriate than a constant friction factor to parametrize frictional decay over the reef.

Wave setup is independent of reef width, while wave height at the shore is inversely proportional to the width. Wave height on the reef flat is shown to depend nearly linearly on the water depth on the reef. The increase of wave height at the shore as the incident wave height increases is attributed primarily to the increase in water depth due to wave setup. Water depth on the reef also affects wave setup with a

slight decrease of wave setup with increasing water level.


The model results demonstrate the importance of water level on the reef flat, hence, the potential effect of sea level rise on wave transformation over this reef would be twofold: higher reef flat water levels would allow more sea and swell energy to reach the shore, but also would result in a moderate decrease in wave setup. For example for Ipan reef, our model results demonstrate that an increase in sea level of 0.5 m over a range of incident wave height of 1 to 5 m yields a decrease of wave setup of 6cm and an increase of SS wave height near the shore of 25 cm.

Appendix

The model defined above is used to evaluate how H_{s1} and $\overline{\eta_1}$, shoreline wave height and wave setup, depend on the three input variables: tidally varying water depth on the reef d_1 and incident wave height H_{s8} .

The independent increase of the three input variables (summarized in Table 1- indep. increase), shown in Fig. 12, demonstrates that the wave setup on the reef flat depends predominantly on offshore wave height. For Ipan, and ignoring the weak effect of wave period and water level, the dependence may be summarized as

$$\overline{\eta_1} = aH_{s8} + b \quad (15)$$

where a and b are parameters constant for a given reef topography. For Ipan, the constants are determined by regression of the model output (runs 300 to 600) and $a \sim 0.26$. The constant b is a negative offset coefficient arising from the fact that if the water at the reef crest is deep enough, no breaking will occur to force wave setup, but for the shallow reef of Guam b is negligible as breaking almost always occurs. Equation (15) is consistent with previous equations relating setup to wave height (Battjes 1974, Gourlay and Colleter 2005, Vetter et al 2010). For comparison with equation 17 of Vetter et al (2010), which relates setup to rms wave height at the breakpoint, $\overline{\eta_1}$ is regressed against the rms wave height at the breakpoint  this results in a slope of 0.32, which compares well with the value of 0.31 from Vetter et al's equation.

From the co-varying increase of both incident wave height and water level, shown in Fig. 13 (summarized in Table 1-co-varying), we determine that the wave height on the reef flat may be written as a monotonic function of the total reef top water depth $h = d_1 + \overline{\eta_1}$

$$H_{s1} = ch^m = c(d_1 + aH_{s8} + b)^m \quad (16)$$

where c and m are positive constants for a given reef topography and may be estimated by regression of the model output on shoreline wave height. The power factor m in equation (16) for Ipan is estimated at $m \sim 1.42$.

Equation (16) applies provided that the reef is submerged everywhere and that the incident waves are larger enough to break on the reef flat.

The effect of variable friction coefficients was tested for Ipan topography by changing the friction coefficients from zero to 4 times the value estimated for Ipan (see summary of parameters in Table 1-var. Cf). The relationship between wave setup and offshore wave height is not significantly affected by changes in friction coefficients. The change of friction however, changes the dependence of reef top wave height on reef top water depth and equation (16) may be rewritten to include the effect of

friction:

$$H_{s1} = c(C_f)(d_1 + aH_{s8} + b(d_1)^{m(C_f)}) \quad (17)$$

The parameters $c(m)$ are decreasing(increasing) for increasing friction but the overall effect is the expected decrease of wave height on the reef flat with increasing friction.

The effect of the width of the reef also was tested with the model (see summary of parameters in table 1- var. L). The wave setup is not significantly changed by a change of reef width and only wave heights on the reef flat are affected by a change in reef width. The wave height near the shoreline is inversely proportional to the width of the reef and equation (17) may be modified to include this dependence

$$H_{s1} = c\left(\frac{C_f}{L}\right)(d_1 + aH_{s8} + b(d_1)^{m(C_f)}) \quad (18)$$

where L is the reef width. This result suggests that the inverse relationship between overwash elevation and adjacent reef width observed by Jaffe and Richmond (1993) may be the results of SS swash oscillations rather the wave setup.

- Baldock TE, Holmes P, Bunker S, van Weert, P (1998) Cross-shore hydrodynamics within an unsaturated surf zone. *Coast Eng* 34:173-196
- Bartholomeusz EF (1958) The reflection of long waves at a step. *Proc Cambridge Philos Soc* 54: 106-118
- Battjes JA (1974) Surf similarity. *Annu Rev Fluid Mech* 20:257-293
- Battjes JA, Janssen JPFM (1978). Energy loss and set-up due to breaking of random waves. Proceedings of the 16th international conference on coastal engineering conference, American Society of Civil Engineers. pp 569-587
- Battjes JA, Bakkenes HJ, Janssen TT, van Dongeren AR (2004) Shoaling of subharmonic gravity waves. *J Geophys Res* 109(C02009) [doi: 10.1029/2003JC001863]
- Bowen AJ, Inman DL, Simmons VP (1968) Wave set-down and wave set-up. *J Geophys Res* 73(8):2569-2577
- Brander RW, Kench PS, Hart D (2004) Spatial and temporal variations in wave characteristics across a reef platform, Warraber Island, Torres Strait, Australia. *Mar Geol* 207(1-4):169-184 [doi: 10.1016/j.margeo.2004.03.014]
- Burbick DR (2005) Guam coastal atlas. Report 114, University of Guam Marine Laboratory.
- Elgar S, Herbers THC, Guza RT (1994) Reflection of ocean surface gravity waves from natural beaches. *J Phys Oceanogr* 24:1503-1511.
- Gerritsen F (1981) Wave attenuation and wave set-up on a coastal reef. Technical report, Look Lab. Univ. Hawaii, Honolulu.
- Gourlay MR (1996a) Wave set-up on coral reefs .1. set-up and wave-generated flow on an idealised two dimensional horizontal reef. *Coast Eng* 27(3-4):161-193
- Gourlay MR (1996b) Wave set-up on coral reefs. 2. set-up on reefs with various profiles. *Coastal Eng* 28(1-4):17-55 [doi: 10.1016/0378-3839(96)00008-7]
- Gourlay MR, Colleter G (2005) Wave-generated flow on coral reefs- an analysis for two-dimensional horizontal reef-tops with steep faces. *Coastal Eng* 52(4):353-387 [doi: 10.1016/j.coastaleng.2004.11.007]

- Guza RT, Thornton EB, Holman RA (1984) Swash on steep and shallow beaches. Proceedings of 19th Coastal engineering conference, American Society of Civil Engineers. pp 708-723
- Hardy TA, Young IR (1996) Field study of wave attenuation on an offshore coral reef. *J Geophys Res* 101(C6):14,311-14,326
- Hearn CJ (1999) Wave-breaking hydrodynamics within coral reef systems and the effect of changing relative sea level. *J Geophys Res* 104(C12):30007-30019
- Hench JL, Leichter JJ, Monismith SG (2008) Episodic circulation and exchange in a wave-drive coral reef and lagoon system. *Limnol Oceanogr* 53(6):2681-2694
- Holman RA, Guza RT (1984) Measuring run-up on a natural beach. *Coastal Eng* 8:129-140
- Huntley DA, Simmonds D, Tatavarti R (1999) Use of collocated sensors to measure coastal wave reflection. *J Waterw Port Coast Ocean Eng* 125(1):46-52
- Jaffe BE, Richmond BM (1993) Overwash variability on the shoreline of Guam during typhoon Russ. Proceedings of the Seventh International Coral reef Symposium, volume 1, pp 257-264
- Jonsson IG (1966) Wave boundary layers and friction factors. Proceedings of 10th Coastal Engineering Conference, American Society of Civil Engineers volume 1, pp 127-148
- Kajiura K (1961) On the partial reflection of water waves passing over a bottom of variable depth. Proceedings Tsunami Meetings 10th Pacific Science Congress, IUGG Monograph, volume 24, pp 206-234
- Karunaratna H, Tanimoto K (1995) Numerical experiments on low-frequency fluctuations on a submerged coastal reef. *Coast Eng* 26:271-289
- Kench PS (1998) Physical processes in an Indian ocean atoll. *J Coast Res* 17(2):155-168
- Kench PS, Brander RW (2006) Wave processes on coral reef flats: Implications for reef geomorphology using Australian case studies. *J Coast Res* 22(1):209-223
- LeMéhauté B (1962) On non-saturated breakers and the wave run-up. Coastal Engineering Conference, American Society of Civil Engineers, pp 77-92
- Lobban CS, Scheffer M (1989) Tropical Pacific island environments. University of Guam Press, second edition
- Longuet-Higgins MS, Stewart RW (1962) Radiation stress and mass transport in gravity waves, with application to "surf beats". *J Fluid Mech* 13:481-504
- Longuet-Higgins MS, Stewart RW (1964) Radiation stress in water waves, a physical discussion with applications. *Deep-Sea Res* 11:529-563
- Lowe RJ, Falter JL, Bandet MD, Pawlak G, Atkinson MJ, Monismith SG, Koseff JR (2005) Spectral wave dissipation over a barrier reef. *J Geophys Res* 110(C04001) [doi: 10.1029/2004JC002711]
- Lugo-Fernandez A, Roberts HH, Wiseman WJ (1998a). Tide effects on wave attenuation and wave set-up on a Caribbean coral reef. *Estuar Coast Shelf Sci* 47(4):385-393
- Lugo-Fernandez A, Roberts HH, Wiseman WJ, Carter BL (1998b) Water level and currents of tidal and infragravity periods at Tague Reef, St. Croix (USVI)}. *Coral Reefs* 17(4):343-349
- Lugo-Fernandez A, Roberts HH, Suhayda JN (1998c) Wave transformations across a Caribbean fringing-barrier coral reef. *Cont Shelf Res* 18(10):1099-1124
- Massel SR, Gourlay MR (2000) On the modelling of wave breaking and set-up on coral reefs. *Coast Eng* 39:1-27
- Mei CC (1989) The applied dynamics of ocean surface waves, volume 1 of Advanced series on ocean engineering, World Scientific.
- Mirfenderesk H, Young IR (2003) Direct measurements of the bottom friction factor beneath surface gravity waves. *Appl Ocean Res* 25:269-287
- Monismith S (2007) Hydrodynamics of coral reefs. *Annu Rev Fluid Mech* 39: 37-55
- Munk WH, Sargent MC (1948) Adjustment of Bikini atoll to ocean waves. *Trans Am Geophys Union* 29:855-860

bathy	Ipan	Ipan	Saipan	Ipan	Ipan	Modified Ipan	Ipan
d_1	15-min tide	15-min tide	15-min tide	0-3 m	0-2 m	0-2 m	0-2 m
H_8	15-min H_s	15-min H_s	15-min H_s	0-8 m	0-6 m	0-5 m	0-5 m
T_8	15-min T_p	15-min T_p	15-min T_p	5-20s	10 s	10 s	10 s

Table 1: Summary of parameters and input variables used for the different cases tested with the model described in the model section

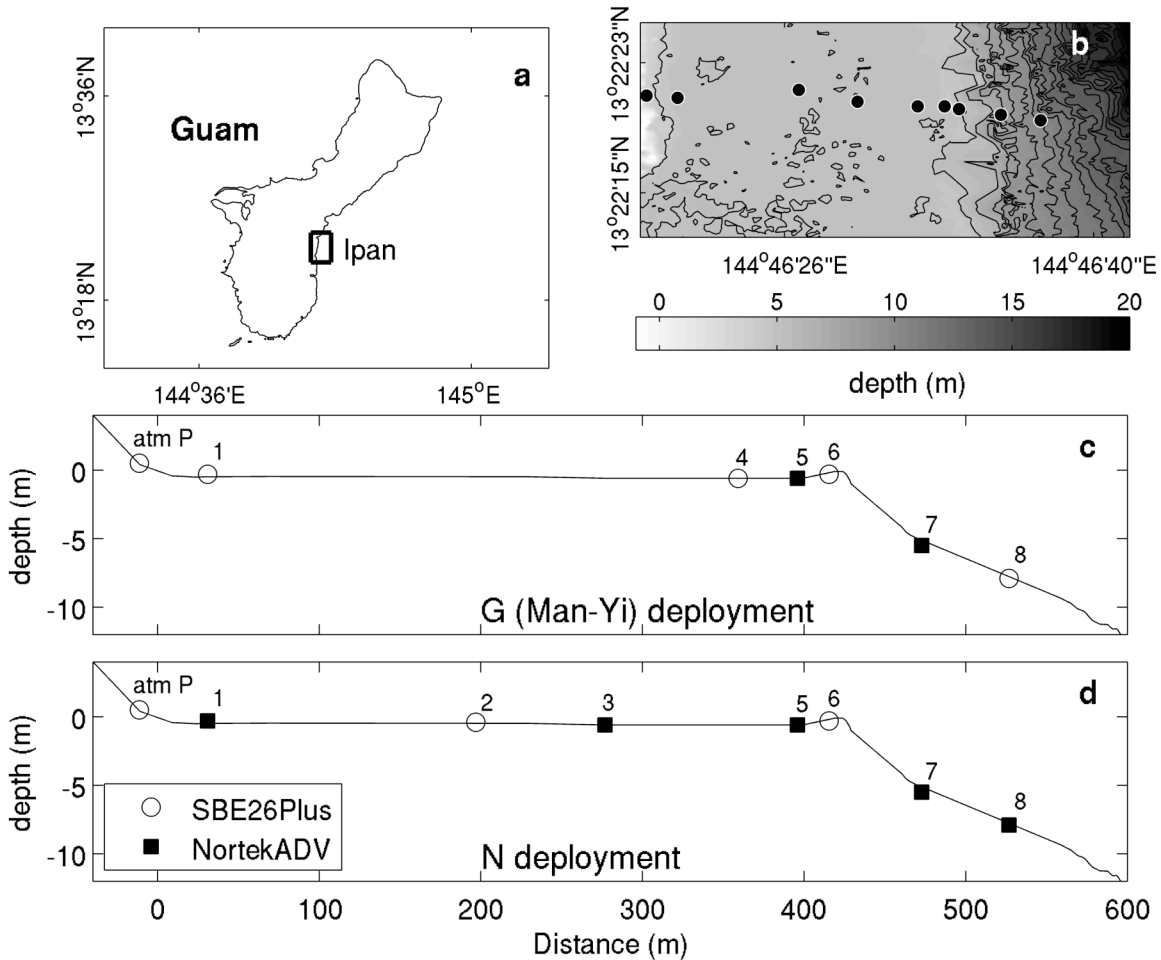
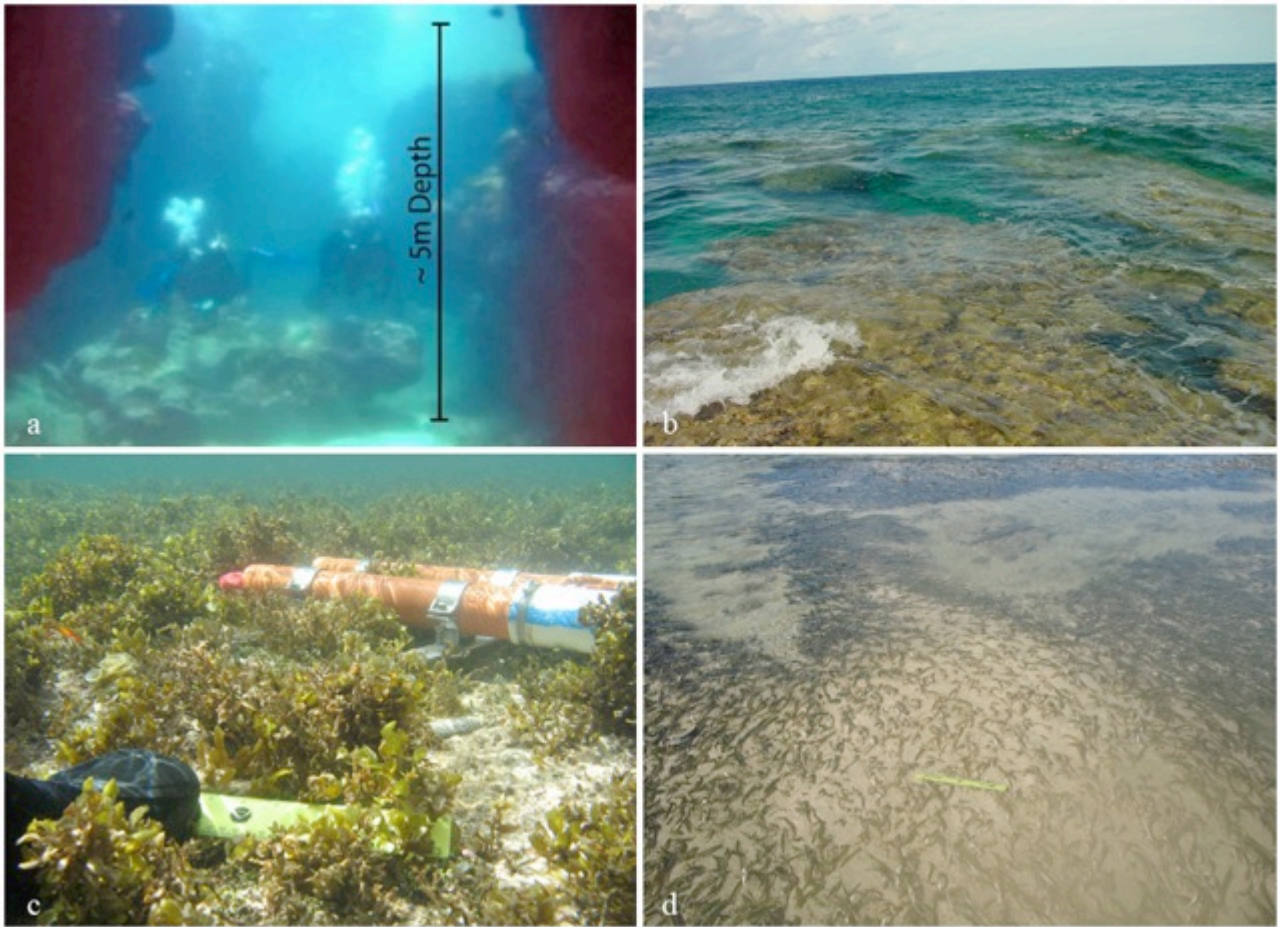


Fig. 1: **a** Location of Ipan reef, Guam. **b** Bathymetry of Ipan reef from SHOALS data with locations of instruments. Cross-shore profile of Ipan reef with locations of sensors for deployment G (June-July 2007) (**c**) and deployment N (September-November 2009) (**d**). Black squares are location of collocated pressure sensors and current-meters. White circles are locations of single pressure sensors at Ipan. The pressure sensor labeled 'atm P' was deployed above sea level to measure the atmospheric pressure.



*Fig. 2: Photos of the substrate for 4 locations across the reef. **a** is near sensor new7 in 5 meters of water, on the spur and groove reef face (scale: divers are ~1.7m tall). **b** is at the reef crest near sensor new6 (scale: the width of the bottom of the photo spans about 3m). **c** is on the reef flat near sensor new4 (scale: the current-meter shown is 60cm long). **d** is on the reef flat near sensor 1 (scale: the yellow ruler is 30cm long).*

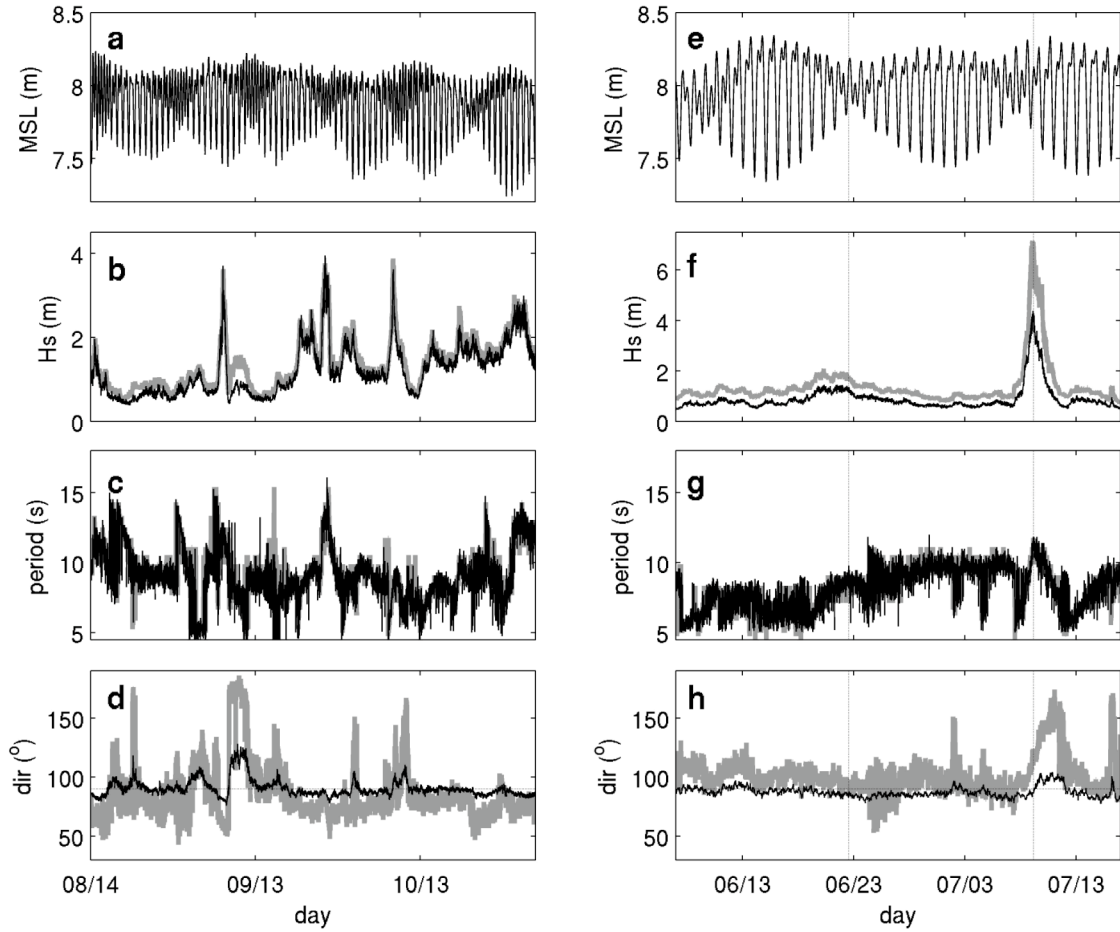
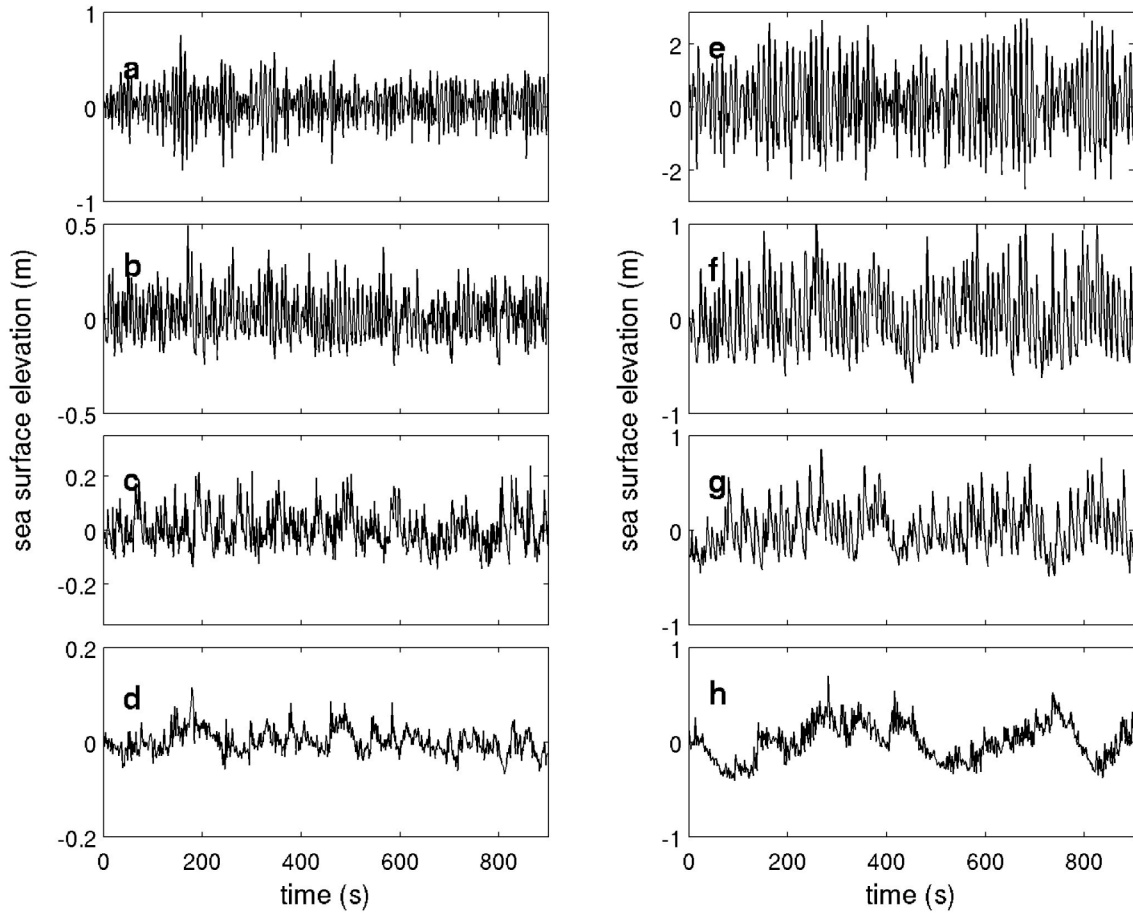
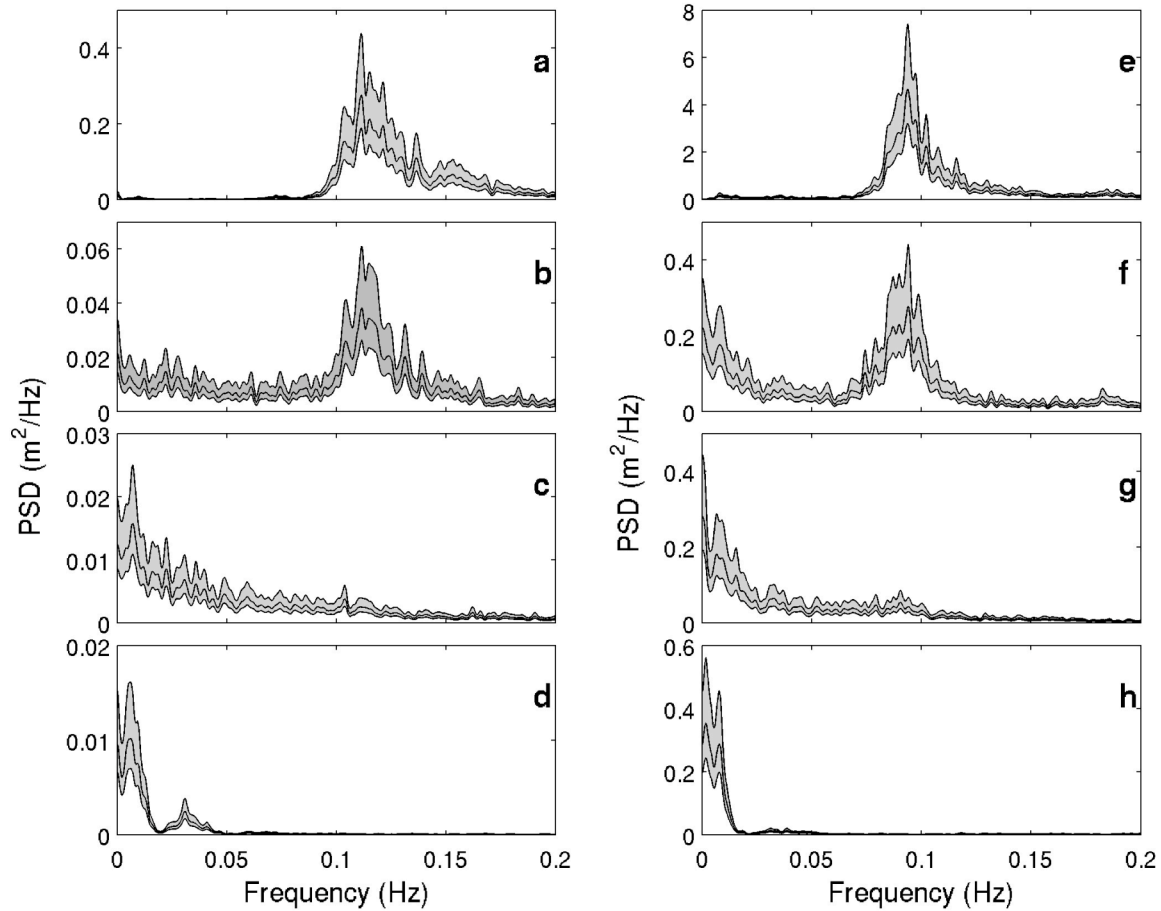


Fig. 3: Conditions during the deployments. Left/right panels show the conditions at Ipan during deployment N (August to November 2009/ the Man-Yi deployment G (June to July 2007) at Ipan. Top panels **a** and **e** show the sea level at the most offshore instrument location. Sub-panels **b** and **f**, **c** and **g** and **d** and **h** show the significant wave height, the peak period and the wave incident angle from the most offshore sensor (black line), and from the CDIP operated offshore buoy (thick grey line). The two vertical dotted lines show the time when the times series of Fig. 4 and the power spectral density of Fig. 5 were collected.



*Fig. 4: 15-minute time series of sea surface elevation at sensor new8 (subplot **a** and **e**), new6 (subplot **b** and **f**), new4 (subplot **c** and **g**) and 1 (subplot **d** and **h**) during a small wave event (left: 22 June 2007 14:00:00) and at the peak of tropical storm Man-Yi (right: 09 July 2007 04:23:00). Wave statistics corresponding to these two events are indicated by the vertical dotted line on Fig. 3.*



*Fig. 5: Examples of power spectral density of sea surface elevation at sensor new8 (subplot **a** and **e**), new6 (subplot **b** and **f**), new4 (subplot **c** and **g**) and 1 (subplot **d** and **h**) during a small wave event (left: 22 June 2007 14:00:00) and the peak of Man-Yi (right: 09 July 2007 04:23:00). Wave statistics corresponding to these two events are indicated by the vertical dotted line on Fig. 3. Spectral properties were estimated based on Fourier transforms of two hour detrended and detided pressure data segments and band averaged using a Parzen spectral window, yielding approximately 44 degrees of freedom and a bandwidth of 0.0016 Hz. The shaded areas show the 95% confidence intervals.*

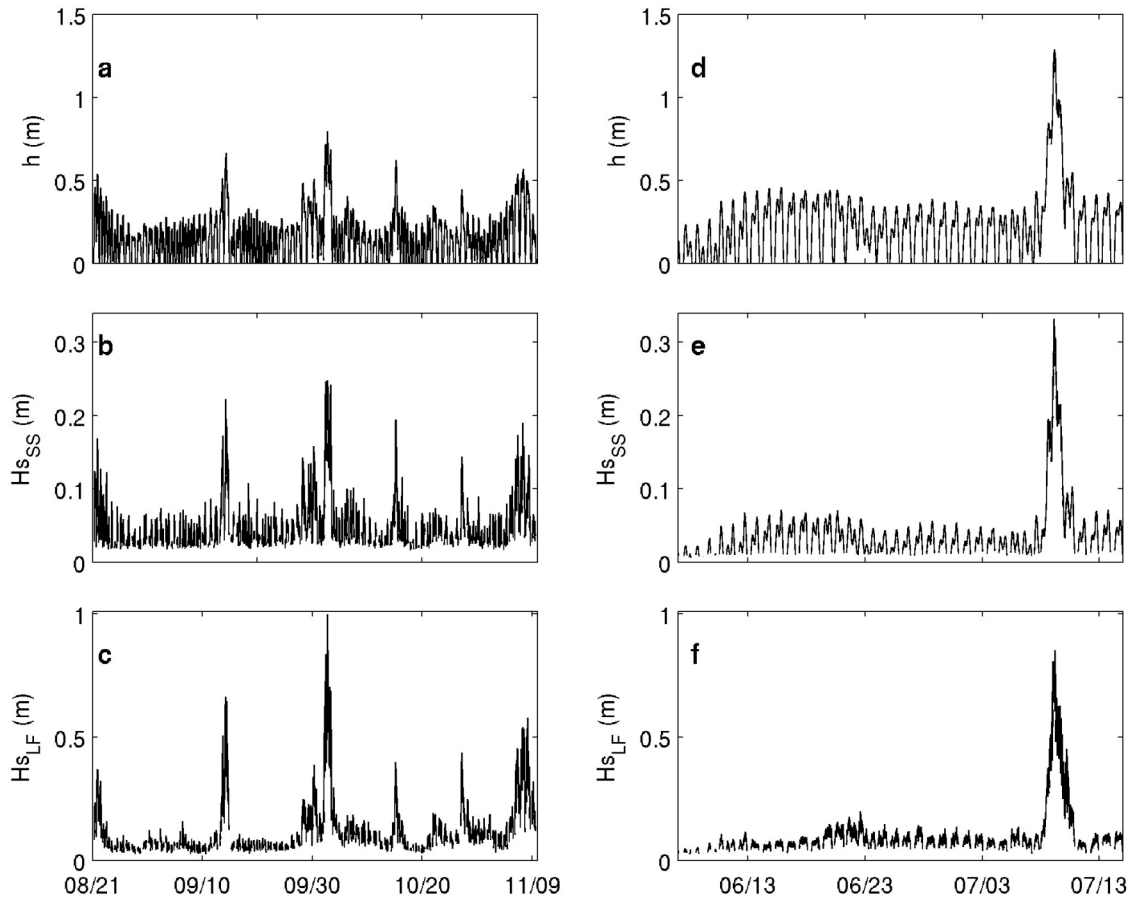


*Fig. 6: Time series of the 15-minute average water depth (**a** and **d**), sea and swell (SS) significant wave height (**b** and **e**) and low frequency (LF=IG+fIG) significant wave height (**c** and **f**) at the nearshore (sensor 1) for deployment N (left) and G (right).*

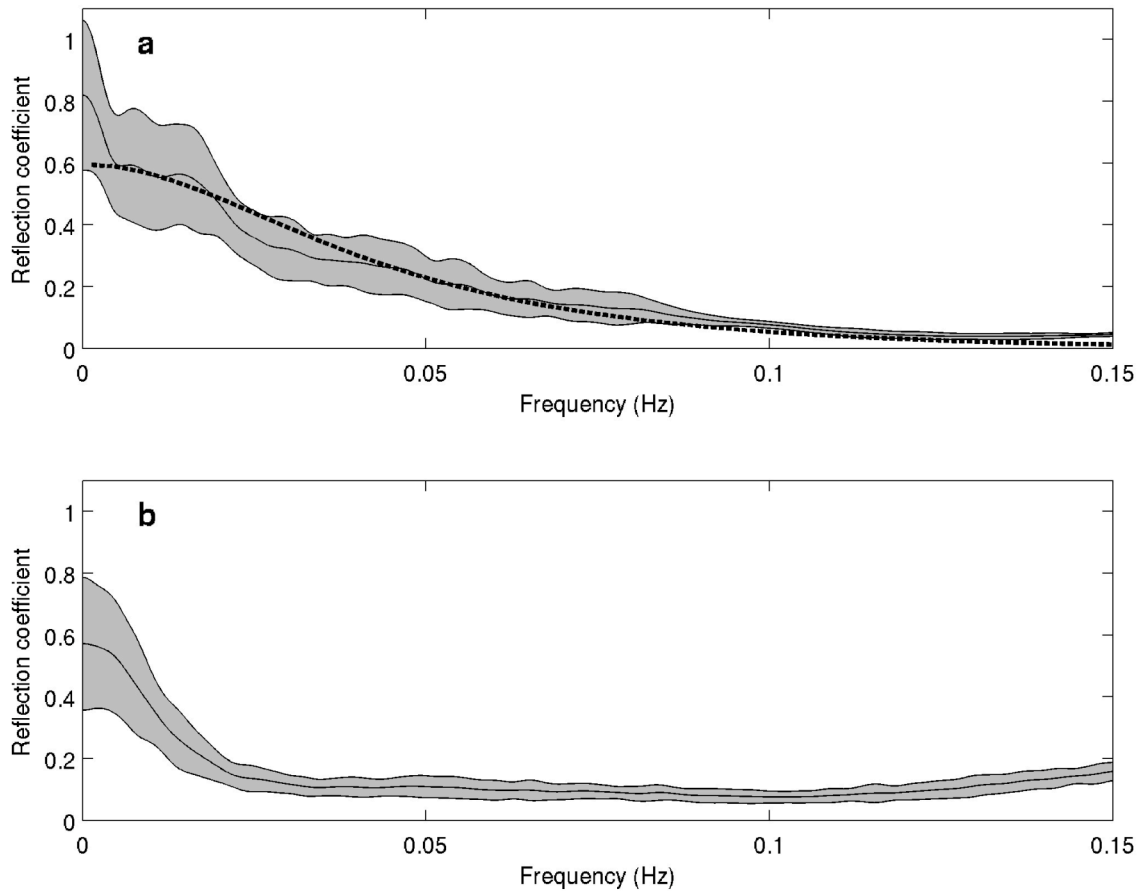


Fig. 7: Ratio of outgoing to incoming energy flux R^2 , as a function of frequency at the reef face (sensor new7, **a**) and on the reef flat (sensor new5, **b**). Grey shading represents the standard deviation around the mean value for the G deployment (June-July 2007). Dash line is theoretical solutions for a smooth step following equations 76 and 79 of (Kajiura 1961) (with $h_1=0.5$ $h_2=30$, $n=2\pi/l=2\pi/40$).

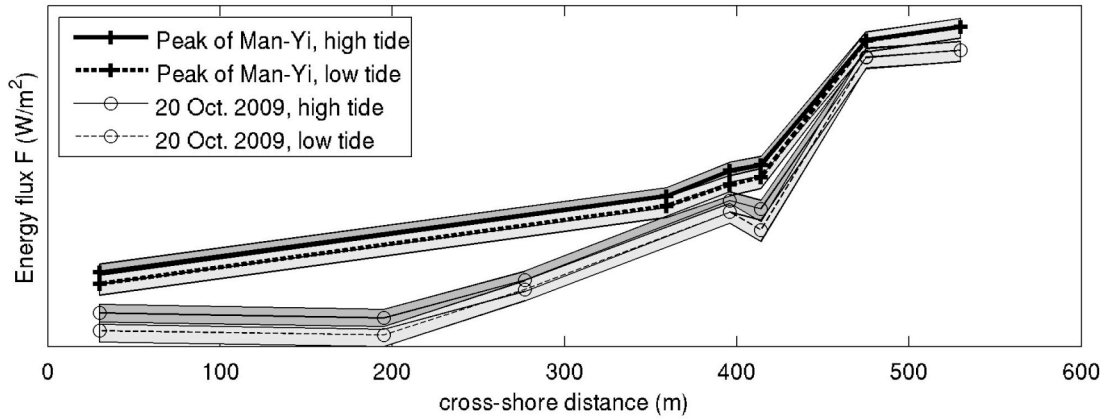


Fig. 8: Examples of net cross-shore energy flux profile across the reef in the sea and swell band for low tide (dash line) and high tide (solid line) at the peak of Man-Yi (thick line) and during the 20 October 2010 wave event (thin line). The shaded areas shows the maximum estimated error from using equation (4) rather than (2), for the low tide (light grey) and high tide (dark grey) .

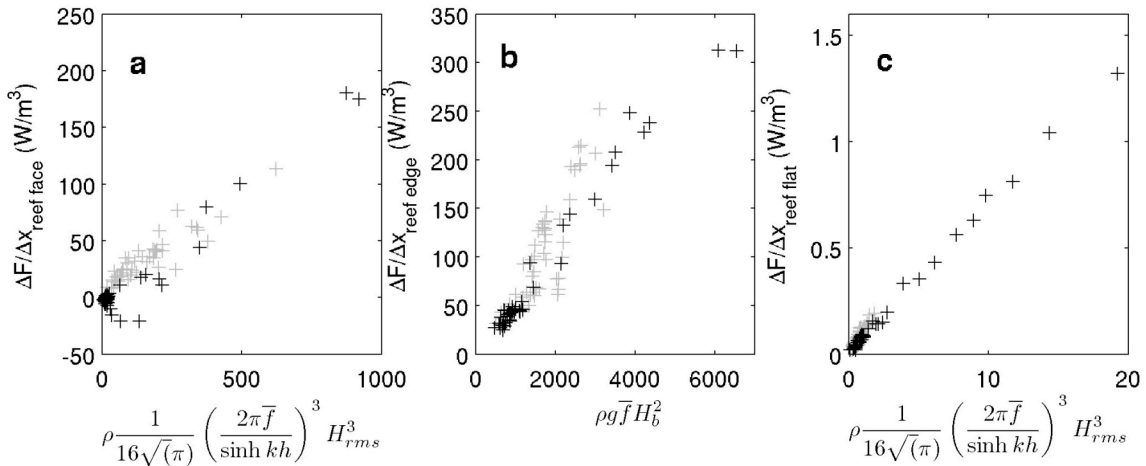


Fig. 9: Average rate of dissipation per unit area on the reef face (**a**, between sensors new8 and new7), over the reef crest (**b**, between sensors new7 and new5) and on the reef flat (**c**, between sensors new4/mew3 (for deployment G/N) and 1) plotted against the best matching parametrization of dissipation. Friction parametrization given by equation (9) for **a** and **c** and breaking parametrization of equation (7) for **b**. Deployment N is shown by the grey + and deployment G is shown with the black +.

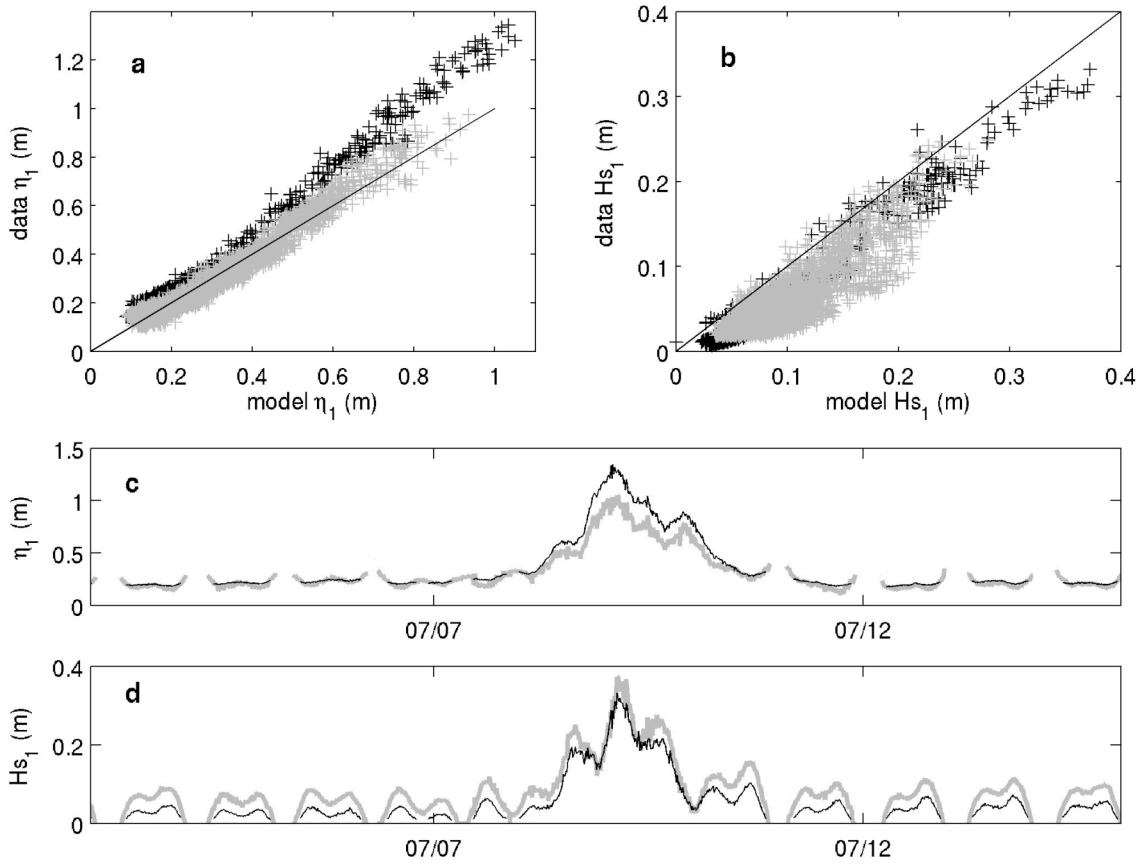


Fig. 10: Comparison of wave setup $\bar{\eta}_1$ (a) and significant wave height H_{s1} (b) at the nearshore sensor (sensor 1) from model (equations (11) to (14)) and data for deployments N (grey crosses) and G (black crosses) (see parameters and inputs in Table 1). Time series of setup $\bar{\eta}_1$ (c) and significant wave height H_{s1} (d) at the peak of tropical storm Man-Yi from model (grey line) and data (black line).

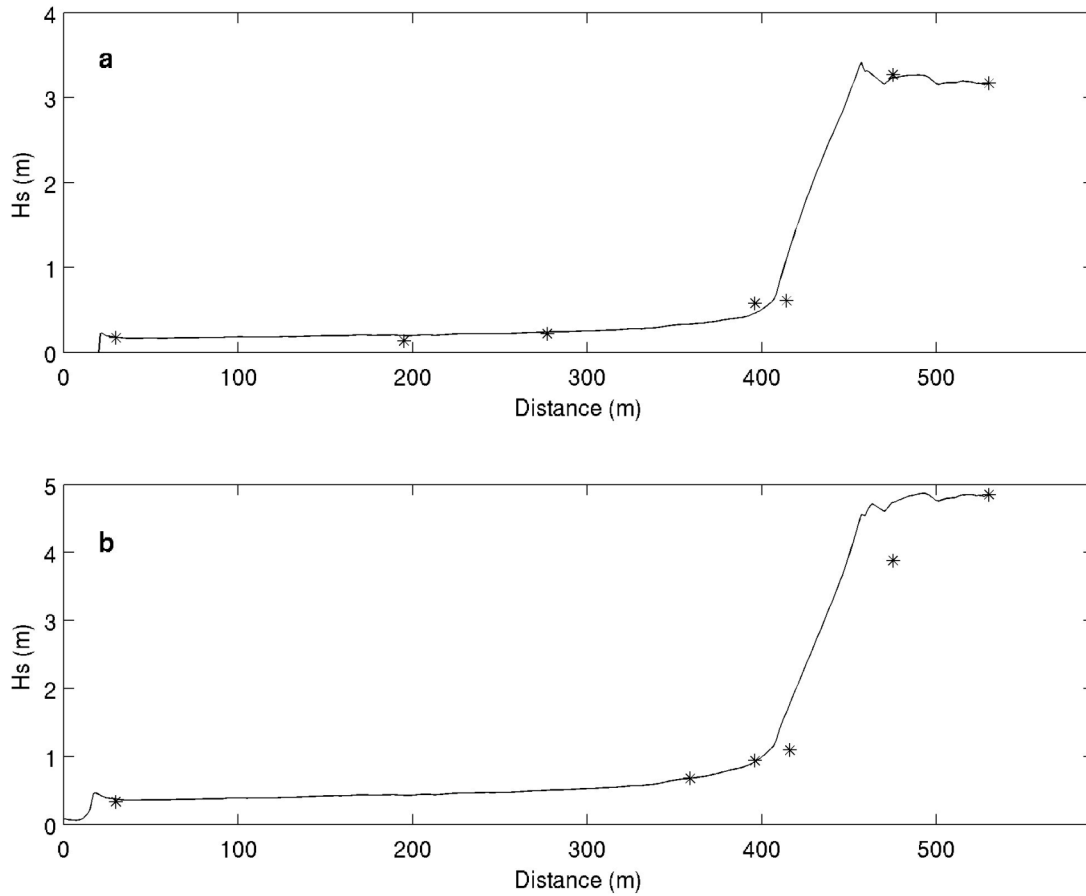


Fig. 11: Comparison of cross-shore profile of significant wave height during a moderate wave event of deployment N (a) and the large wave event at the peak of the storm of deployment G (b) from observed data (stars) and model output (solid line) computed from equations (11) to (14) for Ipan with N and G input variables (see Table 1- N and G).

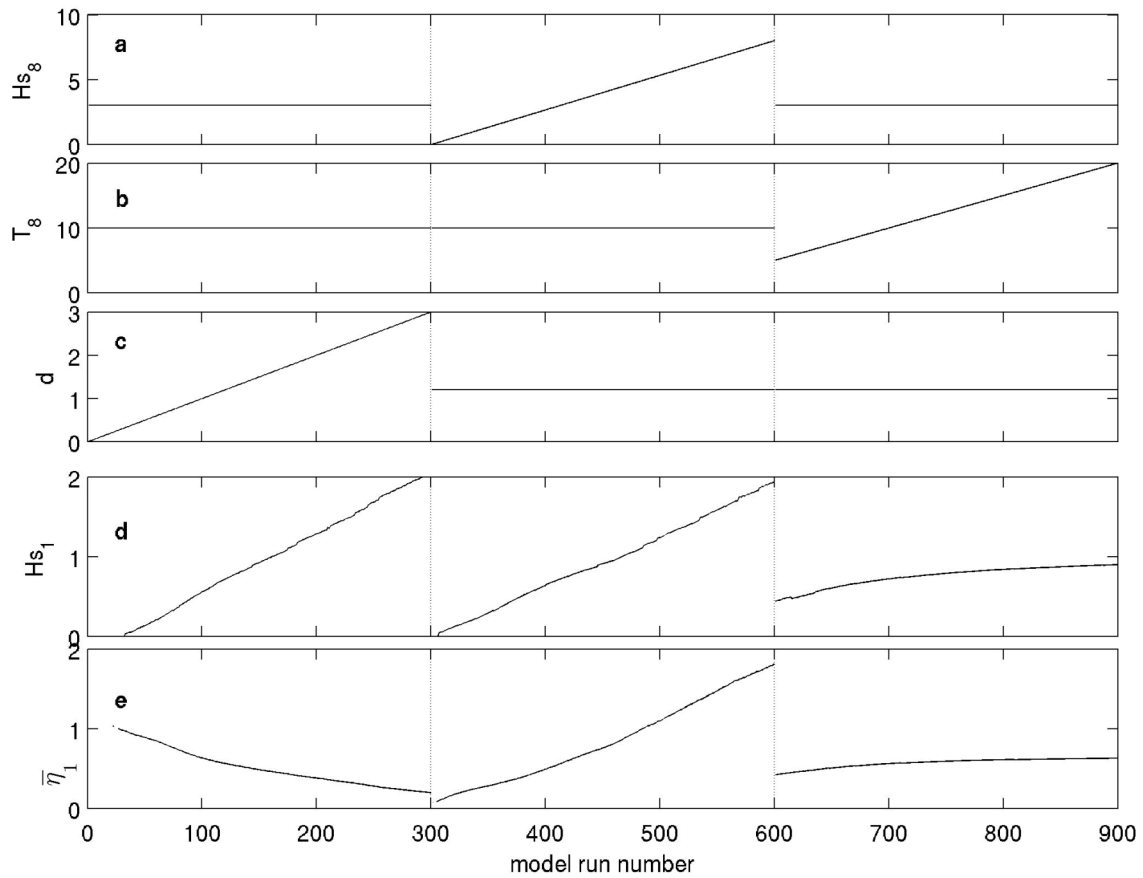


Fig. 12: Model output showing the effect of an independent linear increase in incident wave height, incident wave period and tidal level on near shore sea and swell significant wave height H_{s1} and setup $\bar{\eta}_1$. Parameters used to solved equations (11) to (14) are detailed in Table 1-indep. increase. (a) to (c) input parameters: incident wave height H_{s8} , incident period T_8 and tidal level d . (d) to (f) output parameters: sea and swell significant wave height H_{s1} (d), and setup $\bar{\eta}_1$ (e), at the most inshore location (sensor 1).

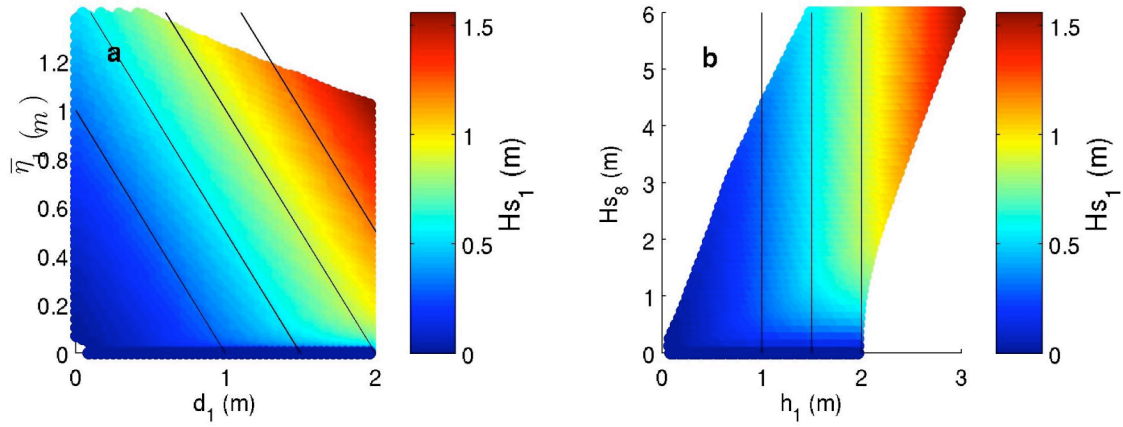


Fig. 13: Effect of co-varying incident wave height and water depth on significant wave height near the shore (H_{s1}) from model output computed from equations (11) to (14) using parameters and input variables summarized in Table 1 (co-varying). **a** the significant wave height at the most inshore sensor H_{s1} as a function of tidal level d and setup $\bar{\eta}$ on the reef at sensor 1. **b** H_{s1} as a function of total depth on the reef h_1 and incident significant wave height H_{s8} . Black lines are line of equal water depth on the reef.

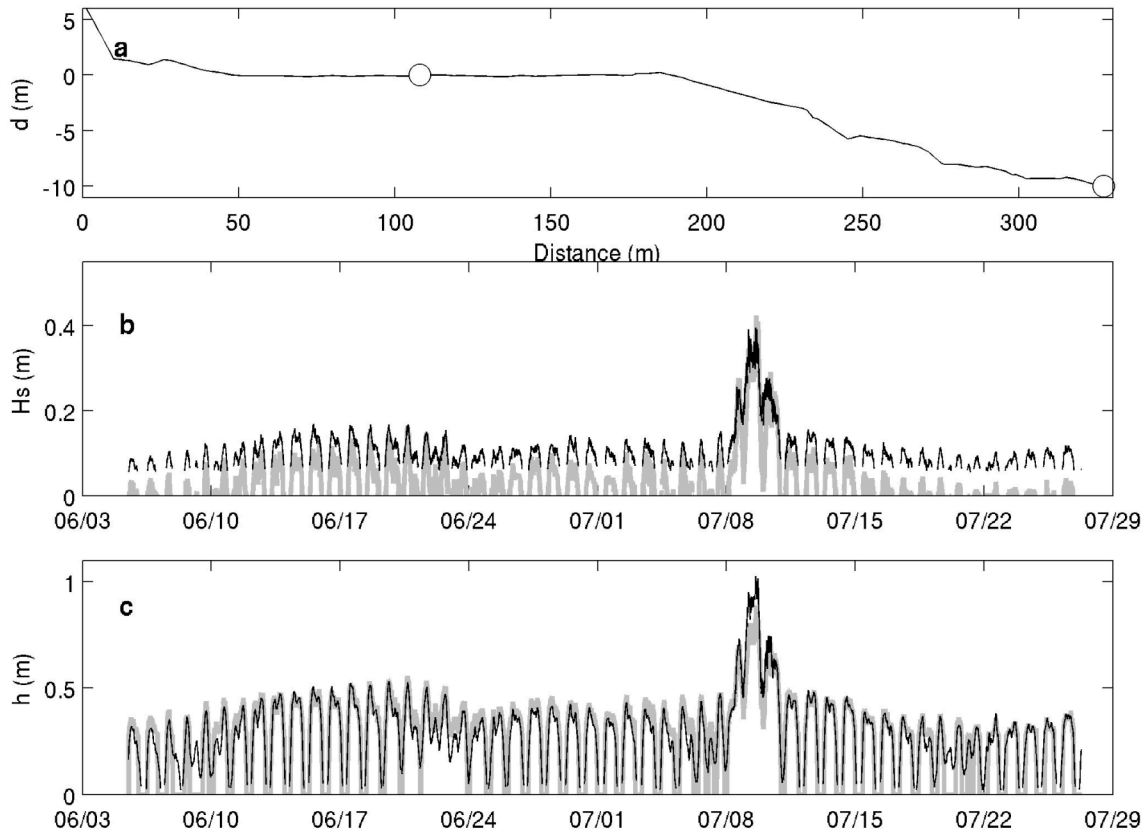


Fig. 14: **a** Cross-shore bathymetry assumed for the Saipan model runs with location of pressure sensors. Comparison of time series of significant wave height H_s (**b**) and total depth h (**c**) at the sensor on the reef flat from data collected at Saipan (black line) and model output (grey line) computed from equations (11) to (14) for Saipan (parameters and input summarized in Table 1- Saipan).

-